materials

MDPI

Article

Study of High-Temperature Behaviour of ZnO by Ab Initio Molecular Dynamics Simulations and X-ray Absorption Spectroscopy

Dmitry Bocharov [1,*], Inga Pudza [1], Konstantin Klementiev [2], Matthias Krack [3] and Alexei Kuzmin [1,*]

[1] Institute of Solid State Physics, University of Latvia, Kengaraga Street 8, LV-1063 Riga, Latvia; inga.pudza@cfi.lu.lv
[2] MAX IV Laboratory, Lund University, P.O. Box 118, SE-221 00 Lund, Sweden; konstantin.klementiev@maxiv.lu.se
[3] Laboratory for Materials Simulations, Paul Scherrer Institut (PSI), CH-5232 Villigen, Switzerland; matthias.krack@psi.ch
* Correspondence: bocharov@cfi.lu.lv (D.B.); a.kuzmin@cfi.lu.lv (A.K.)

Abstract: Wurtzite-type zinc oxide (w-ZnO) is a widely used material with a pronounced structural anisotropy along the *c* axis, which affects its lattice dynamics and represents a difficulty for its accurate description using classical models of interatomic interactions. In this study, ab initio molecular dynamics (AIMD) was employed to simulate a bulk w-ZnO phase in the NpT ensemble in the high-temperature range from 300 K to 1200 K. The results of the simulations were validated by comparison with the experimental Zn K-edge extended X-ray absorption fine structure (EXAFS) spectra and known diffraction data. AIMD NpT simulations reproduced well the thermal expansion of the lattice, and the pronounced anharmonicity of Zn–O bonding was observed above 600 K. The values of mean-square relative displacements and mean-square displacements for Zn–O and Zn–Zn atom pairs were obtained as a function of interatomic distance and temperature. They were used to calculate the characteristic Einstein temperatures. The temperature dependences of the O–Zn–O and Zn–O–Zn bond angle distributions were also determined.

Keywords: ZnO; zinc oxide; ab initio molecular dynamics; extended X-ray absorption fine structure

Citation: Bocharov, D.; Pudza, I.; Klementiev, K.; Krack, M.; Kuzmin, A. Study of High-Temperature Behaviour of ZnO by Ab Initio Molecular Dynamics Simulations and X-ray Absorption Spectroscopy. *Materials* **2021**, *14*, 5206. https://doi.org/10.3390/ma14185206

Academic Editor: Ana Pimentel and Daniela Nunes

Received: 5 August 2021
Accepted: 8 September 2021
Published: 10 September 2021

1. Introduction

Zinc oxide (ZnO) is a wide band-gap (E_g = 3.37 eV) semiconductor, which has a wide range of technological applications, making it an extremely popular research topic in recent years [1–7]. The crystal lattice of the most common ZnO phase belongs to the wurtzite type and is strongly anisotropic [8–10], giving origin to its piezoelectric and pyroelectric properties [11–16].

The unit cell of the wurtzite-type ZnO (w-ZnO) is hexagonal with the space group $P6_3mc$ (186). Each type of atom (Zn or O) forms a hexagonal close-packed sublattice displaced relative to each other along the third-order *c* axis by the parameter *u* [1]. The Wyckoff positions (2*b*) of the Zn and O atoms in the unit cell are Zn (0, 0, 0), (1/3, 2/3, 1/2) and O (0, 0, *u*), (1/3, 2/3, 1/2+*u*). The coordination of each atom in w-ZnO is tetrahedral by four atoms of the other type, and the parameter *u* determines the distortion of the ZnO_4 tetrahedra. The anisotropic structure of ZnO affects its lattice dynamics. In particular, the anisotropy of ZnO thermal expansion and atom thermal vibrations (thermal ellipsoids) along the *a* and *c* axes directions was observed by X-ray diffraction [17–19].

Phonons control all thermal properties of ZnO such as heat capacity, thermal expansion and thermal conductivity [20]. The latter is a key factor responsible for heat dissipation and thus limits the use of ZnO in power electronics applications [21]. Therefore, an understanding of the phonon dynamics in the high-temperature regime is important for the design of ZnO-based devices.

The lattice dynamics of wurtzite-type ZnO was studied in the past by the Zn K-edge X-ray absorption spectroscopy at low temperatures (10–300 K) [22,23]. The information on the thermal disorder and anisotropy effects was extracted using two different simulation approaches, such as classical molecular dynamics and reverse Monte Carlo (RMC), which were both combined with ab initio multiple-scattering (MS) theory. The accuracy of several force-field models [24–26] often used for molecular dynamics simulations of bulk and nanocrystalline ZnO was confirmed by comparing the experimental and simulated Zn K-edge extended X-ray absorption fine structure (EXAFS) spectra. It was found that the existing force-field models cannot accurately describe the correlated atomic motion. At the same time, a more accurate solution was obtained from EXAFS data with the RMC method. In particular, two non-equivalent groups of atoms were resolved in both the first and second coordination shells of the absorbing Zn atom as a result of the ZnO structure anisotropy. An increase in temperature leads to the fact that the structure of ZnO becomes even more anisotropic, which is reflected in a change in the parameter u [22]. As a result, oxygen atoms displace along the c axis, and the Zn–O bond lengths vary [22].

Ab initio molecular dynamics (AIMD) provides an alternative, although computationally more expensive, approach to describe the lattice dynamics in zinc oxide. In this study, we performed AIMD simulations for bulk wurtzite-type ZnO at high temperatures (300–1200 K) and validated the obtained theoretical results by their direct comparison with the experimental Zn K-edge EXAFS spectra.

2. Experimental Details

Polycrystalline wurtzite-type ZnO (99.99% purity, Alfa Aesar, Haverhill, MA, USA) and BN powders were mixed and pressed into a pellet. High-temperature Zn K-edge (9659 eV) X-ray absorption experiments were performed on the BALDER beamline at the 3.0 GeV storage ring of MAX IV Laboratory [27]. The X-ray beam from the in-vacuum wiggler source was monochromatized using a liquid-nitrogen-cooled double-crystal Si(111) monochromator and measured by two ionization chambers located before and after the sample and filled with N_2 and Ar gases. An uncoated Si collimating mirror and silica focusing mirror were used for harmonic reduction. The sample temperature was controlled using the Linkam, 1000 °C furnace.

3. Computational Details

The AIMD simulations of wurtzite-type ZnO were performed within the isobaric-isothermal (NpT) ensemble. The trajectories of atoms were obtained by numerically solving Newton's equations of motion, and the forces between atoms were calculated on-the-fly based on Kohn–Sham density functional theory (DFT) within the Born–Oppenheimer approximation. All simulations were conducted using the QUICKSTEP module [28] of the CP2K code [29,30] at the Swiss National Supercomputing Centre (CSCS, "Piz Daint"). The AIMD simulations were performed at four temperatures: 300 K, 600 K, 900 K and 1200 K. At each temperature, the system was first thermalized for 15 ps, and the atomic configurations were collected during the production (sampling) run of 30 ps duration. The exchange-correlation functional PBEsol [31] was employed in all runs together with Goedecker–Teter–Hutter (GTH) pseudopotentials ([Ar] $4s^2\,3d^{10}$ for Zn and [He] $2s^2\,2p^4$ for O) [32] and contracted Gaussian basis sets of double-zeta quality. The basis sets were specifically optimized for use with the GTH pseudopotentials for the condensed phase systems (DZVP, MOLOPT-SR) [33].

The zinc oxide structure was modelled by a $6a \times 4b \times 4c$ ($a = b = 3.2417$ Å, $c = 5.1876$ Å [19]) supercell, composed of 96 orthorhombic unit cells (Figure 1). Periodic boundary conditions (PBC) were employed in all runs. Note that to avoid artificial correlation effects due to PBC in EXAFS calculations, the maximum cluster radius was set to half of the shortest supercell vector length [34,35]. An orthorhombic unit cell was used because the CP2K/QUICKSTEP implementation works computationally more efficiently

for such supercells that speed up the AIMD simulations. A DFT+U correction [36–38] was applied for all zinc atoms using an effective Hubbard $U_{eff}(Zn)$ of 1.0 eV.

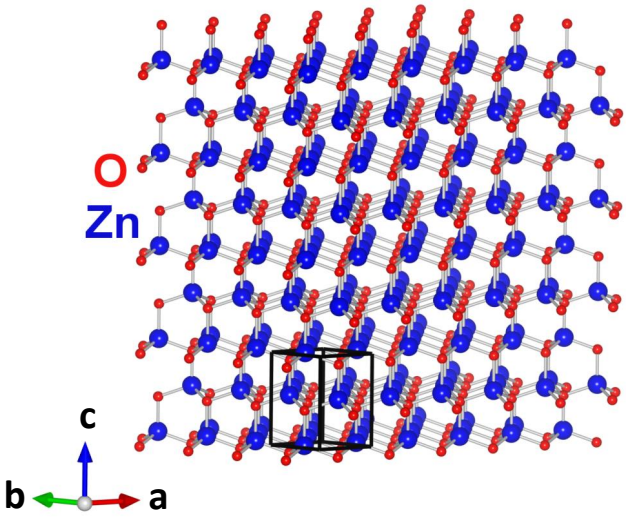

Figure 1. The crystal structure of wurtzite-type ZnO: a supercell $6a \times 4b \times 4c$ used in AIMD simulations is shown. The unit cell is indicated by thick black lines.

An ensemble of uncorrelated atomic configurations retrieved from the AIMD trajectory at each temperature was used to calculate the configuration-averaged Zn K-edge EXAFS $\chi(k)$. Here k is the photoelectron wavenumber defined as $k = \sqrt{(2m_e/\hbar^2)(E - E_0)}$, where m_e is the electron mass, and $\hbar$ is the Planck constant. The origin E_0 of the kinetic energy of the photoelectron was set to obtain the best alignment between the energy scales of the experimental and calculated EXAFS spectra [39]. All EXAFS calculations were performed within the multiple-scattering formalism [34,40] using the ab initio self-consistent real-space MS FEFF8.50L code [41,42]. The cluster with the radius of 8 Å and centred at the absorbing Zn atom was constructed based on the crystallographic ZnO structure and used to obtain the potential and partial phase shifts, required for the calculation of scattering amplitudes in the EXAFS equation [39]. The EXAFS amplitude damping due to the photoelectron inelastic losses was accounted for using the complex exchange-correlation Hedin–Lundqvist potential [43]. The EXAFS amplitude reduction factor S_0^2 was set to 1.0 [39].

4. Results and Discussion

The average lattice parameters obtained using the AIMD calculations in the NpT ensemble increase with temperature and are in agreement with the known experimental values (Table 1). Thus, AIMD simulations reproduce well the thermal expansion of the lattice. Note that there is some scattering in the experimental values of the lattice parameters of ZnO at 300 K [44].

Table 1. The average lattice parameters for ZnO obtained from AIMD simulations using the NpT ensemble vs. the experimental values from [19].

	AIMD		Experiment	
Temperature (K)	***a* (Å)**	***c* (Å)**	***a* (Å)**	***c* (Å)**
300	3.258	5.220	3.24992(5)	5.20658(8)
600	3.265	5.231	3.25682(5)	5.21251(8)
900	3.272	5.243	3.26480(5)	5.21939(8)
1200	3.281	5.257		

The Zn K-edge EXAFS $\chi(k)k^2$ spectra and their Fourier transforms (FTs) calculated at 300, 600, 900 and 1200 K based on the results of the AIMD simulations using the NpT ensemble are shown in Figure 2 in comparison with the experimental data. Note that the peaks in the FTs are located at the distances R which are slightly shorter than crystallographic distances r because the FTs were not corrected for the phase shift present in the EXAFS equation [39]. On the whole, the calculated EXAFS spectra $\chi(k)k^2$ reasonably reproduce the experimental ones at all temperatures. The calculated and experimental EXAFS spectra agree well in phase in k-space as well as in the position of peaks in their FTs in R-space due to the small difference between the lattice parameters, which remains less than 0.02 Å at all temperatures (Table 1).

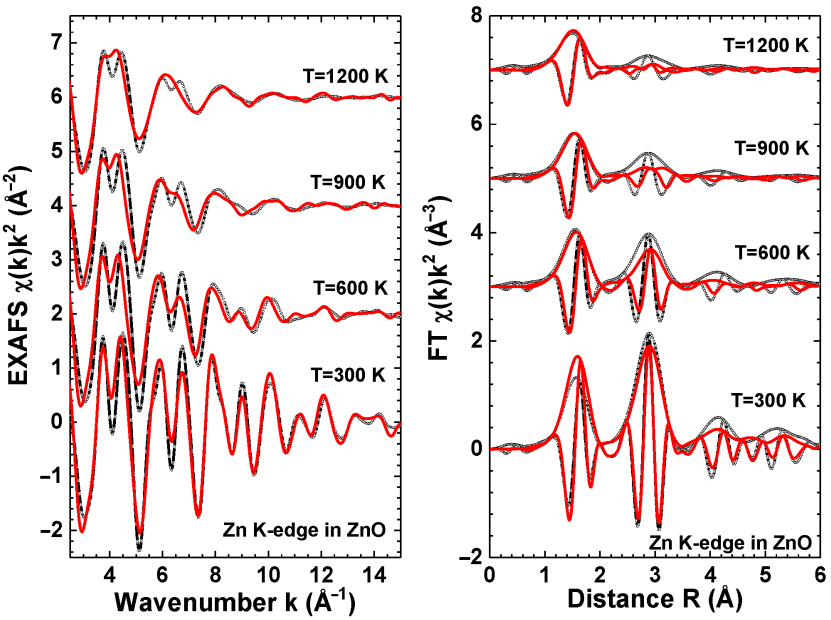

Figure 2. Comparison of the experimental (black curves) and AIMD calculated (red curves) Zn K-edge EXAFS spectra and their Fourier transforms (FTs) at 300, 600, 900 and 1200 K. The AIMD calculations were performed in the NpT ensemble. The curves are shifted vertically for clarity.

An increase in the damping of the EXAFS spectra at large-k values is clearly seen in Figure 2 at higher temperatures and is due to stronger thermal disorder. The comparison of the results in R-space allows for an estimation of the disorder effects in the different coordination shells. As one can see, the experimental and calculated FTs agree well in the first coordination shell of zinc composed of four oxygen atoms (the peak at R = 1.6 Å, uncorrected), however, the thermal disorder is slightly overestimated by AIMD in the outer coordination shells leading to the smaller peak amplitude at large R-values. Some disagreement in the first peak amplitude for T = 300 K can be caused by the remaining contribution of quantum effects (zero-point energy), which is not taken into account in our AIMD simulations and becoming negligible at higher temperatures.

A comparison of the pair distribution functions (PDFs) $g(r)$ for Zn–O and Zn–Zn atom pairs, calculated from the atomic coordinates, are shown in Figure 3. The crystallographic distances at 300 K are indicated by vertical lines [19]. The first coordination shell of zinc is strongly asymmetric at 600, 900 and 1200 K, indicating the anharmonicity of the Zn–O bonding. This result agrees well with the experimental findings by single-crystal neutron diffraction [19].

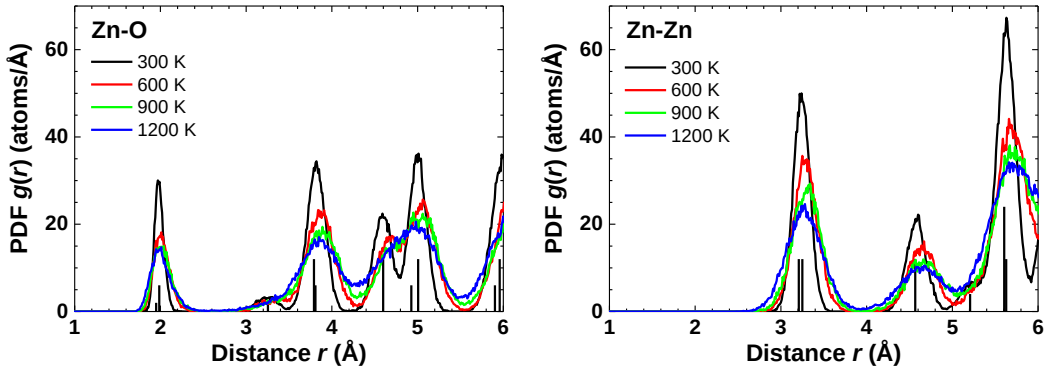

Figure 3. Atomic pair distribution functions (PDFs) around absorbing Zn atom obtained from AIMD calculations in the NpT ensemble at 300, 600, 900 and 1200 K. Vertical lines show crystallographic distances in wurtzite-type ZnO at 300 K from [19].

The atomic coordinates from the AIMD simulations were used to calculate the mean-square relative displacements (MSRDs) σ^2 for each pair of atoms and to follow their distance and temperature dependencies. The values of $\sigma^2(T,r)$ for Zn–O and Zn–Zn atom pairs are shown in Figure 4 (left panel). Note that MSRD values increase with temperature and interatomic distance.

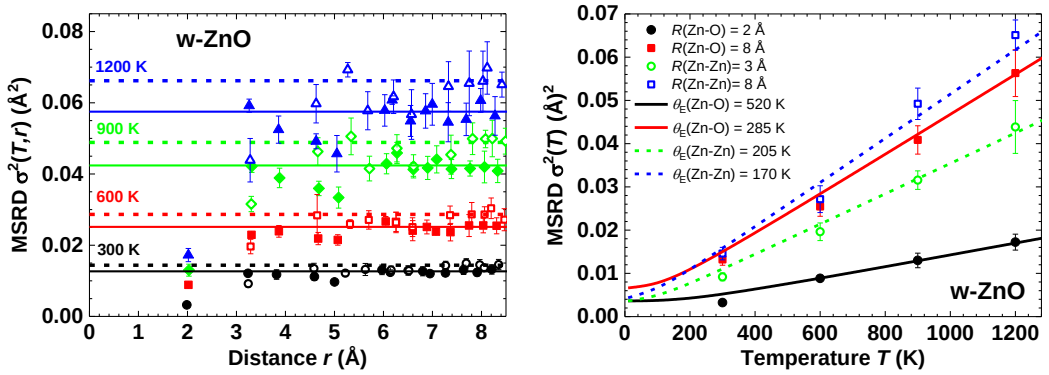

Figure 4. Left panel: Dependence of the Zn–O (solid symbols) and Zn–Zn (open symbols) MSRDs $\sigma(T,r)^2$ on distance R and temperature T in wurtzite-type ZnO evaluated from AIMD calculations at 300 K (circles), 600 K (squares), 900 K (diamonds) and 1200 K (triangles) in the NpT ensemble. Horizontal lines show asymptotic behaviour of MSRDs for distant shells. Right panel: Temperature dependence of MSRD factors for the nearest and distant Zn–O and Zn–Zn atom pairs in w-ZnO. Solid and dashed lines are fits by the Einstein model with the characteristic temperature θ_E for Zn–O and Zn–Zn atom pairs, correspondingly.

It is known that the MSRD value for the pair of atoms i and j is related to their mean-square displacements (MSDs) as $\mathrm{MSRD}_{ij} = \mathrm{MSD}_i + \mathrm{MSD}_j - 2\varphi\sqrt{\mathrm{MSD}_i}\sqrt{\mathrm{MSD}_j}$, where φ is a dimensionless correlation parameter [45,46]. Therefore, the behaviour of MSRDs at large distances ($r \gtrsim$ 5–6 Å) in Figure 4 reflects the disappearance of correlation ($\varphi \xrightarrow{r\longrightarrow\infty} 0$) in the motion of distant atoms [46–49]. Therefore, the asymptotic behaviour of MSRD can be utilized to determine MSD values (Table 2). The MSD values at 300, 600 and 900 K are in agreement with the experimental ones obtained by single-crystal neutron diffraction [19].

Table 2. Temperature dependence of the mean-square displacements (MSDs) for oxygen and zinc atoms in ZnO, estimated from the asymptotic behaviour of MSRDs at large distances.

T (K)	MSD(O) (Å^2)	MSD(Zn) (Å^2)
300	0.0054(4)	0.0072(4)
600	0.010(3)	0.014(3)
900	0.018(5)	0.024(5)
1200	0.024(6)	0.033(6)

The temperature dependencies of the MSRDs for the nearest and distant Zn–O and Zn–Zn atom pairs were fitted using the Einstein model [50] (Figure 4 (right panel)). The obtained values of the characteristic Einstein temperatures θ_E are also reported. Large values of θ_E for the nearest O and Zn atoms reflect stronger interactions in the atomic pairs and correlated motion of atoms. At large distances, the interaction between atoms weakens, and their motion becomes uncorrelated, which is reflected in a significant decrease of θ_E. The difference between the two θ_E values is significantly larger for Zn–O compared to Zn–Zn interactions which is a result of the chemical bonding between the Zn and O atoms.

The local lattice dynamics in wurtzite-type ZnO can also be described by a variation of the O–Zn–O and Zn–O–Zn bond angles within and between ZnO_4 tetrahedra, respectively (Figure 5). One can distinguish two different O–Zn–O (Zn–O–Zn) angles related to the atomic chains located in the *ab* plane or along the *c* axis. The calculated mean values of the two angles at 300 K are about 110° in the *ab* plane and about 108° along the *c* axis, indicating that the Zn atoms are displaced closer to three oxygen atoms located in the basal plane. An increase of temperature leads to the broadening of the bond angle distributions and to a slight decrease of their mean values by about 1° at 1200 K. The obtained values of bond angles at 300, 600 and 900 K are in good agreement with the experimental ones obtained by single-crystal neutron diffraction [19].

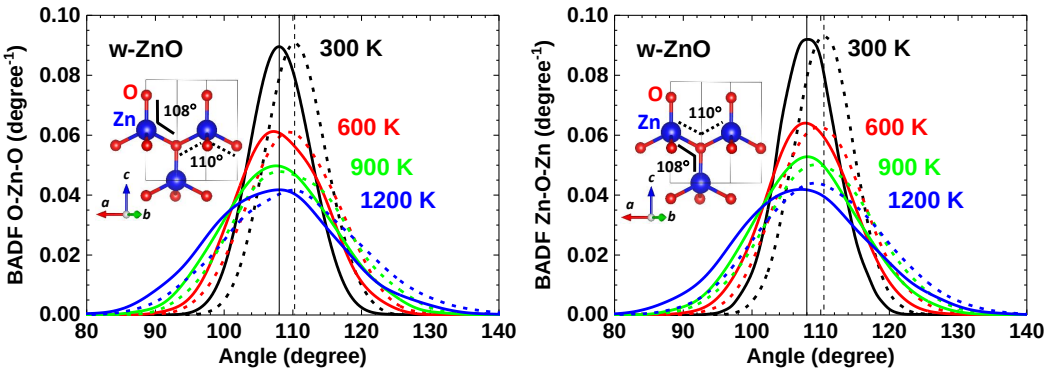

Figure 5. Bond angle distribution functions (BADFs) O–Zn–O and Zn–O–Zn within and between ZnO_4 tetrahedra, respectively, calculated by AIMD. Dashed (solid) curves correspond to the O–Zn–O and Zn–O–Zn angles within the *ab* plane (along the *c* axis). Vertical lines indicate the positions of the distribution maxima at 300 K.

5. Conclusions

AIMD simulations of wurtzite-type ZnO were performed in the NpT ensemble at 300, 600, 900 and 1200 K. The simulation results were validated by comparison with the experimental Zn K-edge EXAFS spectra. Upon increasing temperature, a unit cell expansion occurs in agreement with the available experimental data [19] (Table 1). The obtained atomic configurations were used to calculate the configuration-averaged EXAFS spectra within the multiple-scattering approach [22,23] and are in qualitative agreement with the experimental ones.

Based on the results of the AIMD simulations, the mean-square relative displacements (MSRDs) for Zn–O and Zn–Zn atom pairs and the mean-square displacements (MSDs) for

Zn and O atoms were determined as a function of interatomic distance and temperature. The obtained values of MSDs agree well with those found by single-crystal neutron diffraction [19]. The characteristic Einstein temperatures were determined for Zn–O and Zn–Zn atom pairs from the temperature dependencies of MSRDs.

The PDFs for Zn–O and Zn–Zn show a significant temperature dependence due to the lattice expansion and the amplitude change of the atomic vibrations (Figure 3). An increase of temperature leads to the broadening of the bond angle distributions (Figure 5), whereas the mean values of the bond angles O–Zn–O and Zn–O–Zn remain almost temperature independent. This fact suggests a weak temperature dependence of the parameter u(O) and the piezoelectric coefficients [8]. Our results are in agreement with the conclusions in [19] based on the neutron diffraction measurements in the temperature range of 20–900 K.

Author Contributions: Conceptualization, D.B., M.K. and A.K.; methodology, D.B., K.K. and A.K.; formal analysis, D.B., I.P. and A.K.; investigation, D.B., M.K. and K.K.; visualization, A.K.; validation, D.B., M.K. and A.K.; resources, D.B., K.K. and M.K.; writing—original draft, D.B. and A.K.; writing—review and editing, D.B., I.P., M.K., K.K. and A.K.; funding acquisition, D.B. All authors have read and agreed to the published version of the manuscript.

Funding: Financial support provided by Scientific Research Project for Students and Young Researchers Nr. SJZ/2016/9 realized at the Institute of Solid State Physics, University of Latvia is greatly acknowledged.

Data Availability Statement: The data presented in this study are available in article.

Acknowledgments: D.B., M.K. and A.K. acknowledge access to Piz Daint at the Swiss National Supercomputing Centre, Switzerland (CSCS) under the project ID sm02. The experiment at the MAX IV synchrotron was performed within the project 20190823. Institute of Solid State Physics, University of Latvia as the Center of Excellence has received funding from the European Union's Horizon 2020 Framework Programme H2020-WIDESPREAD-01-2016-2017-TeamingPhase2 under grant agreement No. 739508, project CAMART2.

Conflicts of Interest: The authors declare no conflict of interest. The funders had no role in the design of the study; in the collection, analyses, or interpretation of data; in the writing of the manuscript, or in the decision to publish the results.

Abbreviations

The following abbreviations are used in this manuscript:

AIMD	Ab Initio Molecular Dynamics
BADF	Bond Angle Distribution Functions
DFT	Density Functional Theory
EXAFS	Extended X-ray Absorption Fine Structure
FT	Fourier Transform
MS	Multiple-Scattering
MSD	Mean-Square Displacements
MSRD	Mean-Square Relative Displacements
PDF	Pair Distribution Function
RMC	Reverse Monte Carlo

References

1. Özgür, U.; Alivov, Y.I.; Liu, C.; Teke, A.; Reshchikov, M.A.; Doğan, S.; Avrutin, V.; Cho, S.J.; Morkoç, H. A comprehensive review of ZnO materials and devices. *J. Appl. Phys.* **2005**, *98*, 041301. [CrossRef]
2. Janotti, A.; de Walle, C.G.V. Fundamentals of zinc oxide as a semiconductor. *Rep. Prog. Phys.* **2009**, *72*, 126501. [CrossRef]
3. Lee, K.M.; Lai, C.W.; Ngai, K.S.; Juan, J.C. Recent developments of zinc oxide based photocatalyst in water treatment technology: A review. *Water Res.* **2016**, *88*, 428–448. [CrossRef] [PubMed]
4. Tereshchenko, A.; Bechelany, M.; Viter, R.; Khranovskyy, V.; Smyntyna, V.; Starodub, N.; Yakimova, R. Optical biosensors based on ZnO nanostructures: Advantages and perspectives. A review. *Sens. Actuat. B-Chem.* **2016**, *229*, 664–677. [CrossRef]
5. Gurylev, V.; Perng, T.P. Defect engineering of ZnO: Review on oxygen and zinc vacancies. *J. Eur. Ceram. Soc.* **2021**, *41*, 4977–4996. [CrossRef]

6. Rasmidi, R.; Duinong, M.; Chee, F.P. Radiation damage effects on zinc oxide (ZnO) based semiconductor devices—A review. *Rad. Phys. Chem.* **2021**, *184*, 109455. [CrossRef]
7. Verma, R.; Pathak, S.; Srivastava, A.K.; Prawer, S.; Tomljenovic-Hanic, S. ZnO nanomaterials: Green synthesis, toxicity evaluation and new insights in biomedical applications. *J. Alloys Compd.* **2021**, *876*, 160175. [CrossRef]
8. Abrahams, S.C.; Bernstein, J.L. Remeasurement of the structure of hexagonal ZnO. *Acta Crystallogr. B* **1969**, *25*, 1233–1236. [CrossRef]
9. Reeber, R.R. Lattice parameters of ZnO from 4.2° to 296° K. *J. Appl. Phys.* **1970**, *41*, 5063–5066. [CrossRef]
10. Karzel, H.; Potzel, W.; Köfferlein, M.; Schiessl, W.; Steiner, M.; Hiller, U.; Kalvius, G.M.; Mitchell, D.W.; Das, T.P.; Blaha, P.; et al. Lattice dynamics and hyperfine interactions in ZnO and ZnSe at high external pressures. *Phys. Rev. B* **1996**, *53*, 11425–11438. [CrossRef]
11. Dal Corso, A.; Posternak, M.; Resta, R.; Baldereschi, A. Ab initio study of piezoelectricity and spontaneous polarization in ZnO. *Phys. Rev. B* **1994**, *50*, 10715–10721. [CrossRef] [PubMed]
12. Wang, Z. Novel nanostructures of ZnO for nanoscale photonics, optoelectronics, piezoelectricity, and sensing. *Appl. Phys. A* **2007**, *88*, 7–15. [CrossRef]
13. Hsiao, C.C.; Huang, K.Y.; Hu, Y.C. Fabrication of a ZnO Pyroelectric Sensor. *Sensors* **2008**, *8*, 185–192. [CrossRef] [PubMed]
14. Bdikin, I.K.; Gracio, J.; Ayouchi, R.; Schwarz, R.; Kholkin, A.L. Local piezoelectric properties of ZnO thin films prepared by RF-plasma-assisted pulsed-laser deposition method. *Nanotechnology* **2010**, *21*, 235703. [CrossRef] [PubMed]
15. Yang, Y.; Guo, W.; Pradel, K.C.; Zhu, G.; Zhou, Y.; Zhang, Y.; Hu, Y.; Lin, L.; Wang, Z.L. Pyroelectric Nanogenerators for Harvesting Thermoelectric Energy. *Nano Lett.* **2012**, *12*, 2833–2838. [CrossRef]
16. Goel, S.; Kumar, B. A review on piezo-/ferro-electric properties of morphologically diverse ZnO nanostructures. *J. Alloys Compd.* **2020**, *816*, 152491. [CrossRef]
17. Schulz, H.; Thiemann, K. Structure parameters and polarity of the wurtzite type compounds SiC-2H and ZnO. *Solid State Commun.* **1979**, *32*, 783–785. [CrossRef]
18. Kihara, K.; Donnay, G. Anharmonic thermal vibrations in ZnO. *Can. Mineral.* **1985**, *23*, 647–654.
19. Albertsson, J.; Abrahams, S.C.; Kvick, Å. Atomic displacement, anharmonic thermal vibration, expansivity and pyroelectric coefficient thermal dependences in ZnO. *Acta Crystallogr. B* **1989**, *45*, 34–40. [CrossRef]
20. Serrano, J.; Manjón, F.J.; Romero, A.H.; Ivanov, A.; Cardona, M.; Lauck, R.; Bosak, A.; Krisch, M. Phonon dispersion relations of zinc oxide: Inelastic neutron scattering and ab initio calculations. *Phys. Rev. B* **2010**, *81*, 174304. [CrossRef]
21. Wu, X.; Lee, J.; Varshney, V.; Wohlwend, J.L.; Roy, A.K.; Luo, T. Thermal Conductivity of Wurtzite Zinc-Oxide from First-Principles Lattice Dynamics—A Comparative Study with Gallium Nitride. *Sci. Rep.* **2016**, *6*, 22504. [CrossRef] [PubMed]
22. Timoshenko, J.; Anspoks, A.; Kalinko, A.; Kuzmin, A. Temperature dependence of the local structure and lattice dynamics of wurtzite-type ZnO. *Acta Mater.* **2014**, *79*, 194–202. [CrossRef]
23. Kuzmin, A.; Anspoks, A.; Kalinko, A.; Timoshenko, J. The use of X-ray absorption spectra for validation of classical force-field models. *Z. Phys. Chem.* **2016**, *230*, 537–549. [CrossRef]
24. Lewis, G.V.; Catlow, C.R.A. Potential models for ionic oxides. *J. Phys. C Solid State Phys.* **1985**, *18*, 1149–1161. [CrossRef]
25. Zaoui, A.; Sekkal, W. Pressure-induced softening of shear modes in wurtzite ZnO: A theoretical study. *Phys. Rev. B* **2002**, *66*, 174106. [CrossRef]
26. Kulkarni, A.J.; Zhou, M.; Ke, F.J. Orientation and size dependence of the elastic properties of zinc oxide nanobelts. *Nanotechnology* **2005**, *16*, 2749–2756. [CrossRef]
27. Klementiev, K.; Norén, K.; Carlson, S.; Clauss, K.G.V.S.; Persson, I. The BALDER Beamline at the MAX IV Laboratory. *J. Phys. Conf. Ser.* **2016**, *712*, 012023. [CrossRef]
28. VandeVondele, J.; Krack, M.; Mohamed, F.; Parrinello, M.; Chassaing, T.; Hutter, J. QUICKSTEP: Fast and accurate density functional calculations using a mixed Gaussian and plane waves approach. *Comput. Phys. Commun.* **2005**, *167*, 103–128. [CrossRef]
29. Kühne, T.D.; Iannuzzi, M.; Ben, M.D.; Rybkin, V.V.; Seewald, P.; Stein, F.; Laino, T.; Khaliullin, R.Z.; Schütt, O.; Schiffmann, F.; et al. CP2K: An Electronic Structure and Molecular Dynamics Software Package—Quickstep: Efficient and Accurate Electronic Structure Calculations. *J. Chem. Phys.* **2020**, *152*, 194103. [CrossRef]
30. CP2K Developers Group. 2000–2021. Available online: https://www.cp2k.org (accessed on 5 August 2021)
31. Perdew, J.P.; Ruzsinszky, A.; Csonka, G.I.; Vydrov, O.A.; Scuseria, G.E.; Constantin, L.A.; Zhou, X.; Burke, K. Restoring the Density-Gradient Expansion for Exchange in Solids and Surfaces. *Phys. Rev. Lett.* **2008**, *100*, 136406. [CrossRef]
32. Krack, M. Pseudopotentials for H to Kr optimized for gradient-corrected exchange-correlation functionals. *Theor. Chem. Acc.* **2005**, *114*, 145–152. [CrossRef]
33. VandeVondele, J.; Hutter, J. Gaussian basis sets for accurate calculations on molecular systems in gas and condensed phases. *J. Chem. Phys.* **2007**, *127*, 114105. [CrossRef]
34. Kuzmin, A.; Timoshenko, J.; Kalinko, A.; Jonane, I.; Anspoks, A. Treatment of disorder effects in X-ray absorption spectra beyond the conventional approach. *Rad. Phys. Chem.* **2020**, *175*. [CrossRef]
35. Bocharov, D.; Krack, M.; Rafalskij, Y.; Kuzmin, A.; Purans, J. Ab initio molecular dynamics simulations of negative thermal expansion in ScF_3: The effect of the supercell size. *Comput. Mater. Sci.* **2020**, *171*, 109198. [CrossRef]

36. Anisimov, V.I.; Zaanen, J.; Andersen, O.K. Band theory and Mott insulators: Hubbard U instead of Stoner I. *Phys. Rev. B* **1991**, *44*, 943–954. [CrossRef]
37. Dudarev, S.L.; Manh, D.N.; Sutton, A.P. Effect of Mott-Hubbard correlations on the electronic structure and structural stability of uranium dioxide. *Philos. Mag. B* **1997**, *75*, 613–628. [CrossRef]
38. Rabone, J.; Krack, M. A procedure for bypassing metastable states in local basis set DFT+U calculations and its application to uranium dioxide surfaces. *Comput. Mater. Sci.* **2013**, *71*, 157–164. [CrossRef]
39. Kuzmin, A.; Chaboy, J. EXAFS and XANES analysis of oxides at the nanoscale. *IUCrJ* **2014**, *1*, 571–589. [CrossRef] [PubMed]
40. Kuzmin, A.; Evarestov, R.A. Quantum mechanics–molecular dynamics approach to the interpretation of X-ray absorption spectra. *J. Phys. Condens. Matter* **2009**, *21*, 055401. [CrossRef] [PubMed]
41. Ankudinov, A.L.; Ravel, B.; Rehr, J.J.; Conradson, S.D. Real-space multiple-scattering calculation and interpretation of X-ray-absorption near-edge structure. *Phys. Rev. B* **1998**, *58*, 7565–7576. [CrossRef]
42. Rehr, J.J.; Albers, R.C. Theoretical approaches to X-ray absorption fine structure. *Rev. Mod. Phys.* **2000**, *72*, 621–654. [CrossRef]
43. Hedin, L.; Lundqvist, S. Explicit local exchange-correlation potentials. *J. Phys. C Solid State Phys.* **1971**, *4*, 2064. [CrossRef]
44. Shalimov, A.; Paszkowicz, W.; Grasza, K.; Skupiński, P.; Mycielski, A.; Bak-Misiuk, J. X-ray characterisation of a bulk ZnO crystal. *Phys. Status Solidi B* **2007**, *244*, 1573–1577. [CrossRef]
45. Booth, C.H.; Bridges, F.; Bauer, E.D.; Li, G.G.; Boyce, J.B.; Claeson, T.; Chu, C.W.; Xiong, Q. XAFS measurements of negatively correlated atomic displacements in $HgBa_2CuO_{4+\delta}$. *Phys. Rev. B* **1995**, *52*, R15745. [CrossRef] [PubMed]
46. Jeong, I.K.; Heffner, R.H.; Graf, M.J.; Bilinge, S.J.L. Lattice dynamics and correlated atomic motion from the atomic pair distribution function. *Phys. Rev. B* **2003**, *67*, 104301. [CrossRef]
47. Sapelkin, A.V.; Bayliss, S.C. Distance dependence of mean-square relative displacements in EXAFS. *Phys. Rev. B* **2002**, *65*, 172104. [CrossRef]
48. Jonane, I.; Lazdins, K.; Timoshenko, J.; Kuzmin, A.; Purans, J.; Vladimirov, P.; Gräning, T.; Hoffmann, J. Temperature-dependent EXAFS study of the local structure and lattice dynamics in cubic Y_2O_3. *J. Synchrotron Rad.* **2016**, *23*, 510–518. [CrossRef]
49. Jonane, I.; Anspoks, A.; Kuzmin, A. Advanced approach to the local structure reconstruction and theory validation on the example of the W L_3-edge extended X-ray absorption fine structure of tungsten. *Model. Simul. Mater. Sci. Eng.* **2018**, *26*, 025004. [CrossRef]
50. Sevillano, E.; Meuth, H.; Rehr, J.J. Extended X-ray absorption fine structure Debye-Waller factors. I. Monatomic crystals. *Phys. Rev. B* **1979**, *20*, 4908–4911. [CrossRef]